nature physics

SUPPLEMENTARY INFORMATION

DOI: 10.1038/NPHYS2870

Visualization of electron nematicity and unidirectional antiferroic fluctuations at high temperatures in NaFeAs

E. P. Rosenthal[1], E. F. Andrade[1], C. J. Arguello[1], R. M. Fernandes[2], L. Y. Xing[3], X. C. Wang[3], C. Q. Jin[3], A. J. Millis[1], A. N. Pasupathy[1,$]

[1]Department of Physics, Columbia University, New York NY 10027, USA
[2]School of Physics and Astronomy, University of Minnesota, Minneapolis, MN 55455, USA
[3]Beijing National Laboratory for Condensed Matter Physics, Institute of Physics Chinese Academy of Sciences, Beijing 100190, China

$ Contact: apn2108@columbia.edu

I. Comparisons Between Topographic and Spectroscopic Images in LiFeAs and NaFeAs

Figure S1 displays the topographic image associated with fig. 1b along with STS images at various energies. The C_4 symmetric alkali vacancies maintain their full symmetry over the range of energies measured. Similarly, the iron defects maintain their respective C_2 symmetry aligned with the Li-Li bonds over the range of energies measured. The radial extent of the spectroscopic features associated with each defect is limited to a few lattice constants. Figure S2 shows the topographic image associated with fig. 1c, which has been reproduced in fig. S2b. The iron site defects are identified with red lines, and the spectroscopic features in fig. S2b are seen to originate from these defects, though their size and orientation are uniformly different.

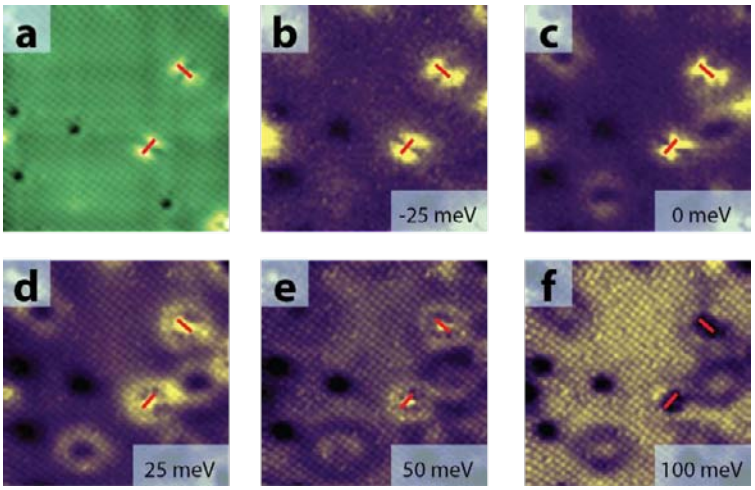

DOI: 10.1038/NPHYS2870

Fig. S1: a, Topographic image of LiFeAs corresponding to the same area as Fig. 1b. Iron site defects are identified by red lines as in the main text. **b**-**f**, Conductance maps corresponding to the same are as **a** and Fig. 1b at various energies. All experimental conditions are the same as Fig. 1b.

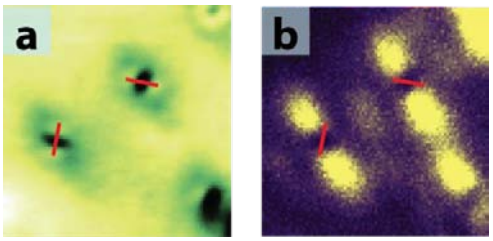

Fig. S2: a, Topographic image of NaFeAs corresponding to same area as Fig. 1c and reproduced here in **b**. Iron site defects are identified with red lines as in the main text.

II. Association of Defects with Spectroscopic Features

Intrinsic defects in NaFeAs are visible in topographic images, as shown in Fig. S3a. By marking each defect from the topography, one may compare the locations of the defects with the locations of unidirectional features seen in simultaneously obtained spectroscopic maps (Fig. S3b, c). There is a clear correlation between the locations of the defects and the unidirectional features, with the unidirectional features appearing centered about the intrinsic defects. Importantly, the spectroscopic feature seen in dI/dV maps is not dependent on the nature of the defect seen in the topography, indicating that the features seen in dI/dV maps are not specific to a particular kind of defect.

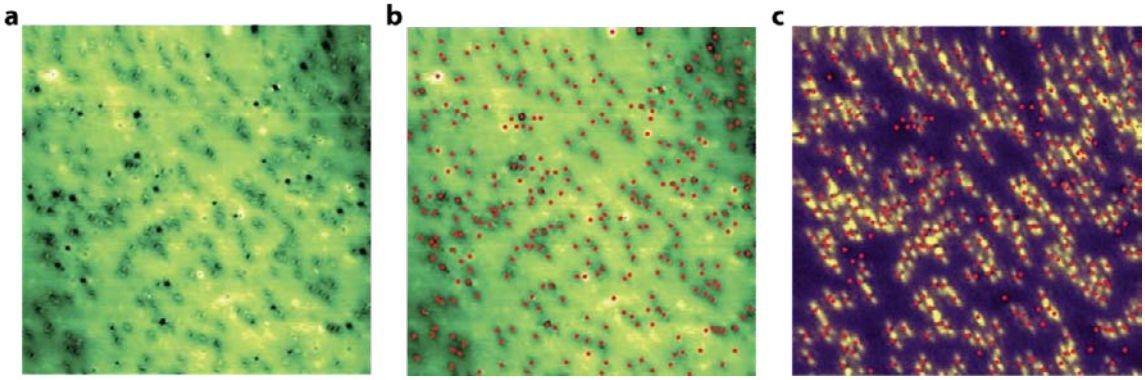

Fig. S3: Comparison between defect locations and spectroscopic, unidirectional features. **a**, Topography at T=26 K showing variety of intrinsic defects. **b**, Same image as **a** but with red dots identifying the location of each defect. **c**, Simultaneously obtained conductance map at E=10 meV with defect locations overlain.

III. Processing of FFT Images

Fourier transform images were processed in order to increase the signal to noise of QPI features. First, drift was removed from STM spectroscopic maps by affine transformation, using

the simultaneously acquired topographic image. After the affine transformation, the conductance images were Fourier transformed. The Fourier image was then mirror symmetrized along the X and Y lattice directions. The images in Fig. 4a-c were additionally low-pass filtered to decrease noise.

IV. Visualization of ARPES Data

The ARPES Fermi surface and joint density of states (JDOS) shown in Fig. 4 are fits to raw data from ref. 1 on NaFeAs along the Γ-X and Γ-Y directions in all three phases – tetragonal paramagnetic (TPM), orthorhombic paramagnetic (OPM), and spin density wave (SDW). A comparison of the published ARPES data and the fitted model in the SDW state are shown in Fig. S4 a and b, respectively. The Fermi surface and corresponding JDOS for the TPM phase, as well as the Fermi surface used for the OPM JDOS in Fig. 4g, is shown in Fig. S5.

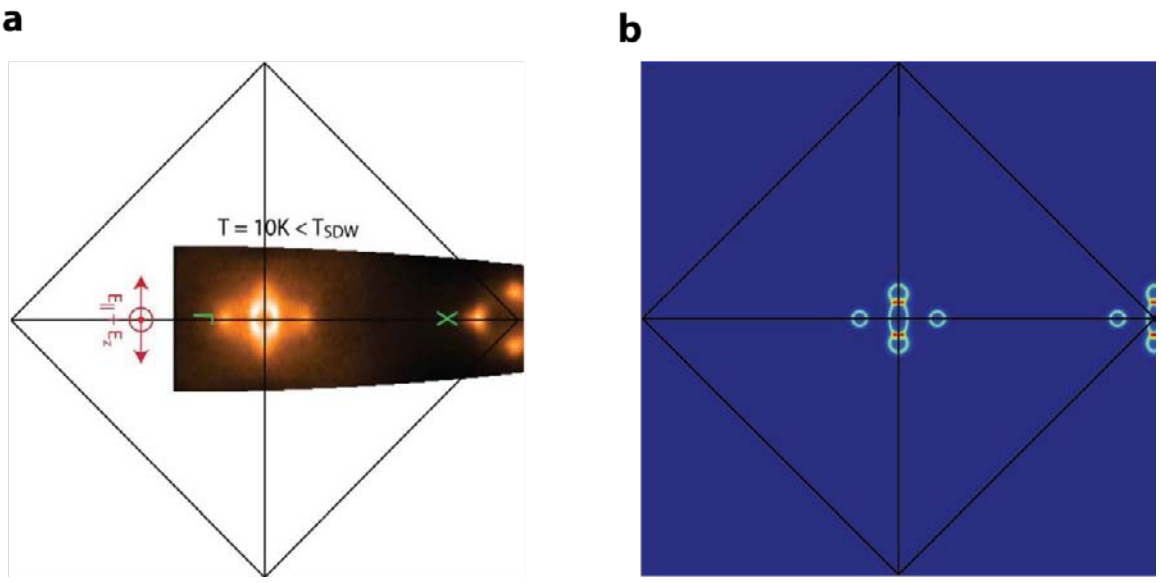

Fig. S4: Comparison between ARPES data and model. **a**, ARPES Fermi surface from ref. 1. Black box corresponds to two Fe Brillouin Zone. **b**, Model Fermi surface generated from curves fit to **a**.

DOI: 10.1038/NPHYS2870

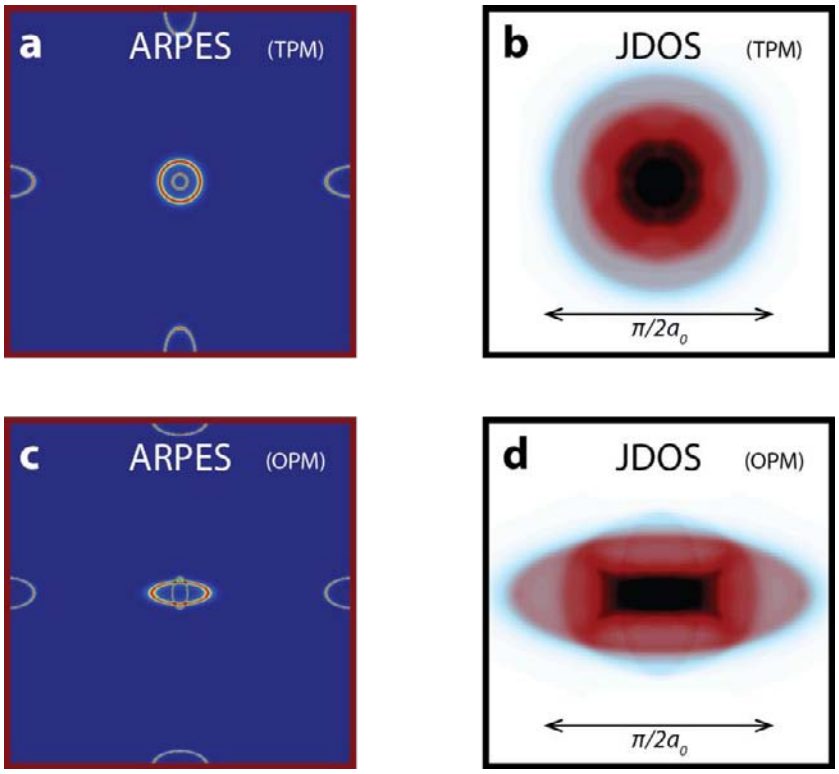

Fig. S5: ARPES Fermi surface and JDOS for tetragonal paramagnetic (TPM) and orthorhombic paramagnetic (OPM) phases. **a**,**b**, TPM ARPES Fermi surface from reference ref. 1. and corresponding JDOS calculated by autocorrelation. **c**,**d**, OPM Fermi surface and JDOS.

V. Calculation of $|\delta n(\boldsymbol{q})|$ for Figure 5

In order to calculate the theoretical quasiparticle interference (QPI) in Fig. 5b, we used Eq. 1 with the T-matrix restricted to the leading and quadratic order in the impurity potential *V*:

$$T(\boldsymbol{k}, \boldsymbol{k}+\boldsymbol{q}; \omega) = V(\boldsymbol{q}) + \int d\boldsymbol{p}\, V(\boldsymbol{p}) G(\boldsymbol{k}+\boldsymbol{p}, \omega) V(\boldsymbol{q}-\boldsymbol{p}) + \cdots$$

For simplicity, we consider a two-band model with a circular hole pocket and an elliptical electron pocket separated by the SDW ordering vector $\boldsymbol{Q}$:

$$\varepsilon_{1,\boldsymbol{k}} = \epsilon_1 - \frac{k^2}{2m}$$

$$\varepsilon_{2,\boldsymbol{k}+\boldsymbol{Q}} = -\epsilon_2 + \frac{k_x^2}{2m_x} + \frac{k_y^2}{2m_y}$$

such that $G_a^{-1} = \omega - \varepsilon_{a,\boldsymbol{k}} + i0^+$ in the paramagnetic tetragonal state. We used the parameters $\epsilon_1 = \epsilon_2$, $m_x = 2m_y$, and $\sqrt{m_x m_y} = 1.01m$. In the SDW state, the normal part of the Green's function is given by:

$$G_a = \frac{\omega - \varepsilon_{\bar{a}}}{(\omega - E_1)(\omega - E_2)}$$

where:

$$E_{1,2} = \left(\frac{\varepsilon_1 + \varepsilon_2}{2}\right) \pm \sqrt{\left(\frac{\varepsilon_1 - \varepsilon_2}{2}\right)^2 + M^2}$$

are the quasi-particle excitation energies and M is the magnetic order parameter set to $M = 0.1\sqrt{\epsilon_1 \epsilon_2}$. The resulting Fermi surfaces for both the normal and SDW state are shown below in Fig. S5.

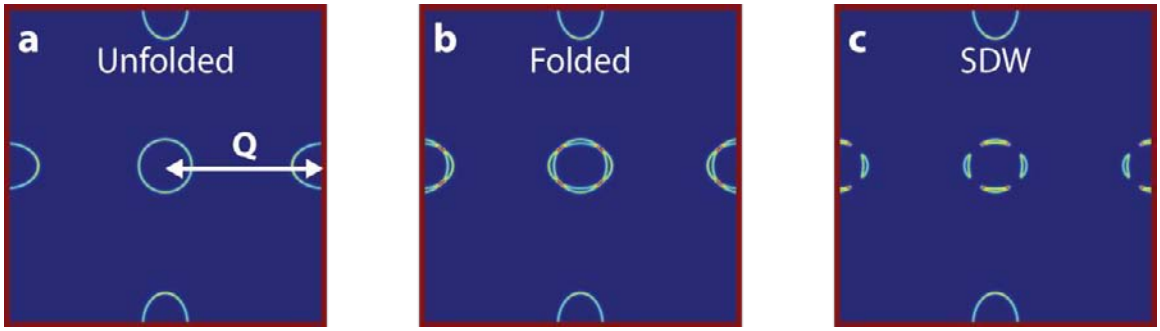

Fig. S6: Fermi surfaces for two-band model. **a**, First Brillouin zone for single Fe unit cell. A circular hole pocket is at the center, and elliptical electron pockets are at the Brillouin zone edge which is located a distance $\boldsymbol{Q}$ from the zone center. **b**, Brillouin zone folded by SDW ordering vector $\boldsymbol{Q}$**.** (**C**) First Brillouin zone in the presence of long-range SDW order. Gaps are opened in regions nested by the SDW ordering vector.

As was mentioned in the text, we consider two possible scenarios of magnetic correlations in the paramagnetic phase: a magnetic droplet and short-range SDW order. In the former case, the impurity potential $V(\boldsymbol{q})$ is peaked at the SDW ordering vector $\pm\boldsymbol{Q}$:

$$V_\sigma(\boldsymbol{q}) = \frac{1}{2}\left(\frac{\lambda}{|\boldsymbol{q} - \boldsymbol{Q}|^2 + \lambda^2} + \frac{\lambda}{|\boldsymbol{q} + \boldsymbol{Q}|^2 + \lambda^2}\right)\sigma$$

Here, σ is a spin index, indicating that the droplet potential has a directional dependence. Because of this, summing over spin indices cancels the linear term in Eq. (S1), and we need to consider the term quadratic in V. In our calculations, we used $\lambda = 0.2k_F$.

In the case of short-range magnetic order in the paramagnetic phase, we consider the Lee-Rice-Anderson (*2*) Green's function:

$$\tilde{G}_a^{-1} = G_a^{-1} - \frac{M^2}{\omega - \varepsilon_{\bar{a}} + i\xi^{-1}}$$

where ξ is proportional to the magnetic correlation length. We fix M to have the same value as in the SDW phase. We consider two particular situations: one with a finite ξ and the other in the limit $\xi \to \infty$. The latter is equivalent to the case of long-range SDW order *without* the coherence factors that mix the hole and electron states. Except in the magnetic droplet case, the impurity potential is assumed to be that of a point impurity, i.e. independent of $\boldsymbol{q}$.

DOI: 10.1038/NPHYS2870

Within this model, we obtain Fig. 5b for the $\xi = 8$ short-range SDW QPI. This image is repeated in Fig. S7 where we include the other three scenarios: $\xi \to \infty$, long-range SDW order, and magnetic droplet. The corresponding real space density of states (DOS) has been plotted next to each respective scenario. Not only is it clear that the short-range SDW order in the paramagnetic phase can produce similar QPI to that of the long-range order, but the unidirectional spectroscopic features seen in real space are qualitatively similar to the real space calculated QPI. Conversely, the magnetic droplet model bears no resemblance to either the calculated long-range SDW QPI or the STS data.

One of main features of the experimental QPI spectrum is the existence of maxima located at angles of ~45° to the Fe-Fe bonds (Fig 4a), which persist up to high temperatures. They can be visualized in a more transparent way via the constant-k_y cut shown in Fig. 4h (correspondent to the dotted orange line in Fig. 4a), which displays maxima at $k_x=0$ and $k_x=q_{D,x}$. Our calculated QPI also displays the same maxima in the SDW phase (see Fig. S6e). Our results reveal that, in the paramagnetic phase, these maxima only appear if the magnetic correlation length overcomes a certain threshold – otherwise, there is only the maximum at $k_x=0$. This is shown in Fig. 5d, where the theoretical constant-k_y cut correspondent to the dotted orange line in Fig. 5c is plotted for several different values of ξ. As the magnetic correlation increases, the maximum is displaced from $k_x=0$ to $k_x=q_{D,x}$. For the case of a magnetic droplet, the maximum remains at $k_x=0$. Thus, the experimental QPI is consistent with the presence of strong unidirectional magnetic fluctuations.

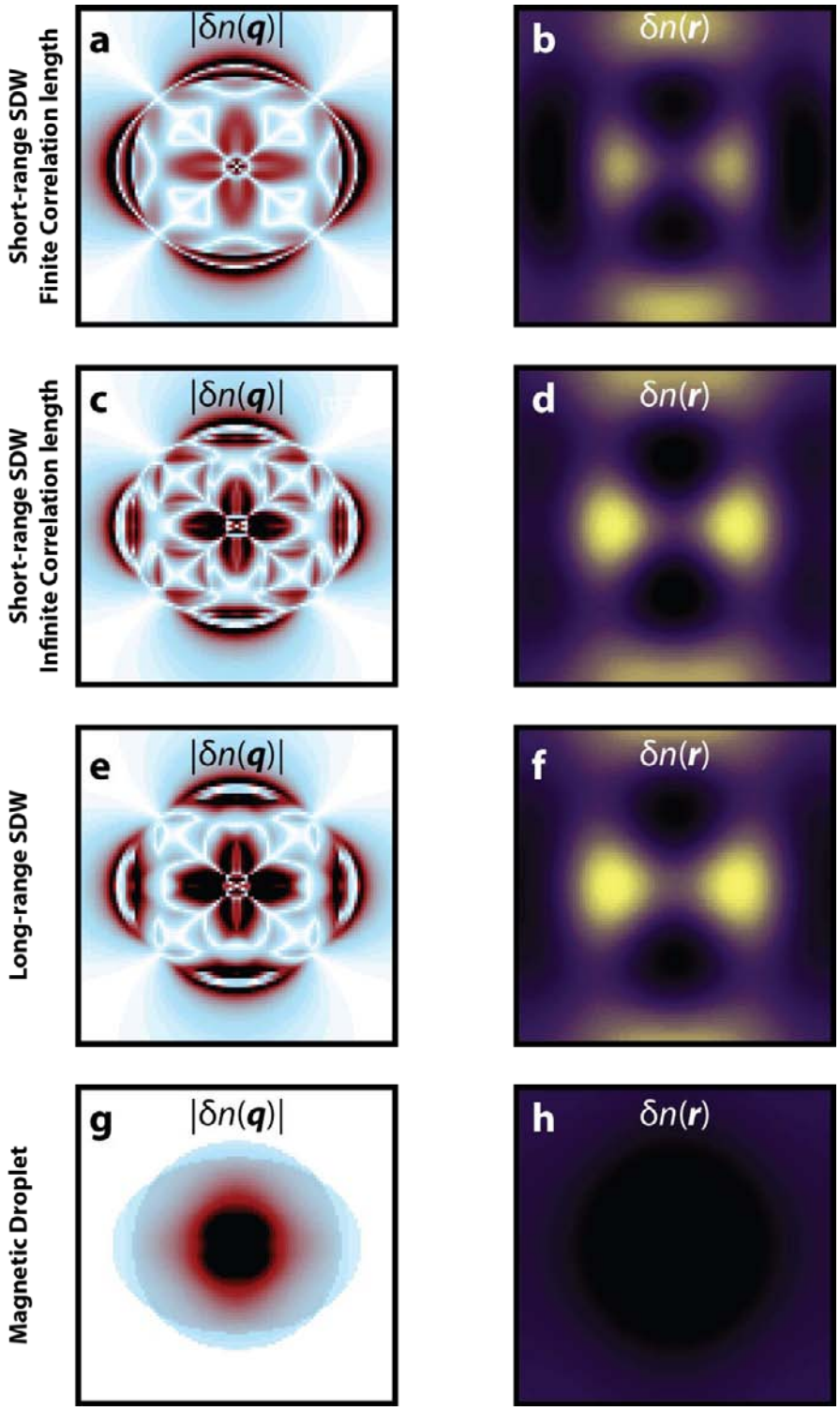

Fig. S7: Models of QPI with magnetic order. Fourier space DOS is on the left, and real space DOS is on the right. **a**,**b**, Short-range SDW order using Lee-Rice-Anderson Green's function for correlation length $\xi = 8$. **c**,**d**, Same model as **a** and **b** but $\xi \to \infty$. **e**,**f**, Long-range SDW order. Real space DOS shows same unidirectional quality as short-range SDW calculations and STS measurements. **g**,**h**, Magnetic droplet calculation.

DOI: 10.1038/NPHYS2870

VI. Generation of Anisotropy Maps and Anisotropy Parameter

All conductance maps were first upconverted to four times the original spatial resolution. Defects were identified, and a circular area of diameter 6.7nm was cropped around each defect. All cropped defects were averaged together to create a supercell image of the average defect appearance for each energy and temperature. The supercells were then C_2 symmetrized. The anisotropy maps were calculated by taking the difference of the supercell and the supercell rotated by 90^{o}. The anisotropy maps were then normalized by first summing the rotated and unrotated supercell and then summing over all values. The anisotropy parameter was calculated by taking the absolute value of the rotated and unrotated supercell difference, summing all values, and dividing by the same normalization used in the anisotropy maps. A perfectly C_4 symmetric would not change under 90^{o} rotation and would yield an anisotropy parameter of zero. Alternatively, a maximally C_2 symmetric image would yield an anisotropy parameter of one.

References

1 Yi, M. *et al. New Journal of Physics* **14**, (2012).
2 Lee, P. A., Rice, T. M. & Anderson, P. W. *Phys Rev Lett* **31**, 462-465, (1973).